Research article

Ze-Peng Zhuang[a], Rui Chen[a], Zhi-Bin Fan, Xiao-Ning Pang and Jian-Wen Dong*

High focusing efficiency in subdiffraction focusing metalens

https://doi.org/10.1515/nanoph-2019-0115
Received April 12, 2019; revised June 1, 2019; accepted June 7, 2019

Abstract: Vector beams with phase modulation in a high numerical aperture system are able to break through the diffraction limit. However, the implementation of such a device requires a combination of several discrete bulky optical elements, increasing its complexity and possibility of the optical loss. Dielectric metalens, an ultrathin and planar nanostructure, has a potential to replace bulky optical elements, but its optimization with full-wave simulations is time-consuming. In this paper, an accurate and efficient theoretical model of planar metalens is developed. Based on this model, a twofold optimization scheme is proposed for optimizing the phase profile of metalenses so as to achieve subdiffraction focusing with high focusing efficiency. Then, a metalens that enables to simultaneously generate radially polarized beam (RPB) and modulate its phase under the incidence of *x*-polarized light with the wavelength of 532 nm is designed. Full-wave simulations show that the designed metalens of NA = 0.95 can achieve subdiffraction focusing (FWHM = 0.429λ) with high transmission efficiency (77.6%) and focusing efficiency (17.2%). Additionally, superoscillation phenomenon is found, leading to a compromise between the subdiffraction spot and high efficiency. The proposed method may provide an accurate and efficient way to achieve sub-wavelength imaging with the expected performances, which shows a potential application in super-resolution imaging.

Keywords: metalens; subdiffraction focusing; vector beam; optimization.

1 Introduction

A sharp focus is crucial for plenty of optical devices, for instance, optical microscopy [1], lithography [2], optical trapping [3], and laser processing equipment [4]. To focus light into a tighter spot, radially polarized beam (RPB) combined with high numerical aperture (NA) has shown great superiority [5–7]. A series of seminal papers have investigated its unique focusing properties through a single focusing lens with or without a pupil filter [8–16]. Compared to spatially uniform polarizations, such as linear and circular polarizations, RPB with an annular filter can be focused into a shaper spot thanks to the significant strong longitudinal electric field component [5, 6]. Subdiffraction focal spots have been also demonstrated by focusing RPB through binary phase pupil filters and a high-NA lens [13, 14]. However, the implementation of such devices requires a combination of several discrete optical elements, including polarization converter, pupil filter and optical lens [8–16]. These conventional optical components are generally bulky, have low efficiency and difficult to manufacture with high precision, hampering the miniaturization and integration of optical devices.

In recent years, dielectric metasurfaces have emerged as a proper candidate to replace bulky optical components due to their compact structure and low dissipation loss. By arranging regular dielectric nanoposts on a subwavelength scale, dielectric metasurfaces could accomplish manipulation of polarization and/or phase of the transmitted light. A large number of metasurface-based devices in both near-infrared and visible regimes have been presented, such as lenses [17–21], beam deflection [22–24], holograms [25–27] and special beam generation [28–35]. Among these devices, focusing metasurfaces, i.e. metalenses, can possibly replace the bulky elements in optical systems to achieve a tight focal spot. Several high-NA metalenses with high resolution have been reported [17–21]. However, the resolutions of these metalenses are still diffraction-limited. Superoscillatory lens using circularly polarized beam has been demonstrated to break the diffraction limit [36], but it suffers from high intensity of side lobes. Considering the unique properties

[a]**Ze-Peng Zhuang and Rui Chen:** These authors contributed equally to this work.
***Corresponding author: Jian-Wen Dong,** School of Physics and State Key Laboratory of Optoelectronic Materials and Technologies, Sun Yat-sen University, Guangzhou 510275, China, e-mail: dongjwen@mail.sysu.edu.cn. https://orcid.org/0000-0003-2379-554X
Ze-Peng Zhuang, Rui Chen, Zhi-Bin Fan and Xiao-Ning Pang: School of Physics and State Key Laboratory of Optoelectronic Materials and Technologies, Sun Yat-sen University, Guangzhou 510275, China

of RPB, a single-layer metalens has been proposed to simultaneously generate RPB and focus it into a tight spot of 0.502λ [32] and the size of the focal spot is compressed down to 0.428λ in the near-infrared regime later [37].

From the above-mentioned studies, it was found that metalenses are able to break diffraction limit. However, the efficiency of them still remains a universally concerned issue [38–40]. To achieve a tighter spot and higher focusing efficiency simultaneously or a balance between them, optimization method based on an accurate modelling of metalens is required. Full-wave simulation has shown very high precision, but it is really time-consuming. To reduce simulation time, some optimization approaches are based on the diffraction theory associated with bulky lenses whose curved surfaces are different from the planar structure of metalenses [17–21, 37]. Consequently, the optimized design based on these methods is not compatible with the metalens itself, resulting in a mismatch with the targeted optimization performance [37]. Therefore, there is an increasing need to develop a theoretical model of metalens from which the performance of metalenses could be predicted more accurately.

In this paper, a dielectric single-layer metalens with subdiffraction focusing is proposed. A theoretical model of metalens is developed and combined with binary particle swarm optimization (BPSO) algorithm to optimize the phase profile of metalenses. According to the optimized phase profile, a 20 μm diameter dielectric titanium dioxide metalens with NA = 0.95 at the wavelength of 532 nm is designed. The designed metalens can achieve subdiffraction focusing (FWHM = 0.429λ) with high focusing efficiency (17.2%). It is also shown that the theoretical results agree well with full-wave simulations, providing a fast design method of metalens without tedious numerical simulations. The impacts of the superoscillation phenomenon in the super resolution and focusing efficiency are also discussed. Such design method shows potential in achieving super-resolution imaging in an integrated and efficient way.

2 Structures to achieve polarization and phase control simultaneously

A schematic illustration of the designed dielectric single-layer metalens is showed in Figure 1. It integrates the functionalities of the traditional bulky optical elements (Figure 1A), including polarization converter, binary

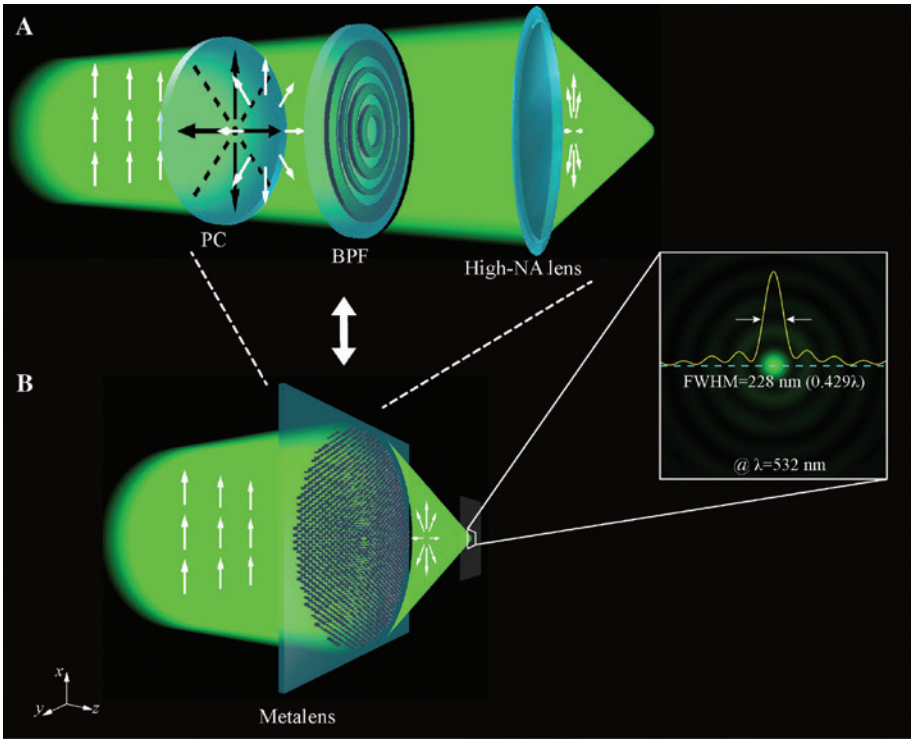

Figure 1: Schematic illustration of subdiffraction focusing metalens with *x*-polarized incident light.
(A) The traditional focusing system, including three discrete optical elements, a polarization converter, a binary phase filter (BPF), and a high-NA lens. It can be implemented by a single-layer metalens in (B). The designed metalens, consisting of a hexagonal array of dielectric nanoposts, can achieve a subdiffraction spot of FWHM 0.429λ at a wavelength of 532 nm, which is reflected in the right inset.

phase filter (BPF) and high-NA lens into a lightweight and compact device. As seen from Figure 1B, a *x*-polarized beam at the wavelength of 532 nm can be focused to a subdiffraction spot through the designed metalens. The metalens composes of a hexagonal array of titanium dioxide rectangle nanoposts standing on the silicon dioxide substrate. The unit cell of the periodic array in Figure 2A is characterized by lattice constant a, width, length and height of the nanoposts, W, L, H, and rotational angle θ. For fixed height of nanoposts, H, the rotational angle θ accounts for polarization change as shown in Figure 2B while a combination of width, W, and length, L, of a nanopost for the phase delay of transmitted light.

To show the capability of complete polarization and phase control, rigorous coupled-wave theory [41] is adopted to simulate the periodic array. As an example, a periodic array consisting of rectangle nanoposts with $L=255$ nm, $W=117$ nm, $H=900$ nm, $\theta=0$ and $a=320$ nm is simulated. Normalized magnetic intensity is shown in Figure 2C. The magnetic field is mainly confined in the nanoposts and each nanopost can be regarded as a weakly coupled low-quality-factor Fabry-Pérot resonator [30]. Therefore, the response of each nanopost is independent and the effect from neighboring nanoposts can be neglected. Figure 2D shows the phase distribution when the *x*- and *y*-polarized incident light transmit the nanopost, indicating a phase difference π for the two orthogonal *x*- and *y*-polarized incident light. As a result, each nanopost can be approximated as an independent half-wave plate, with a Jones matrix form:

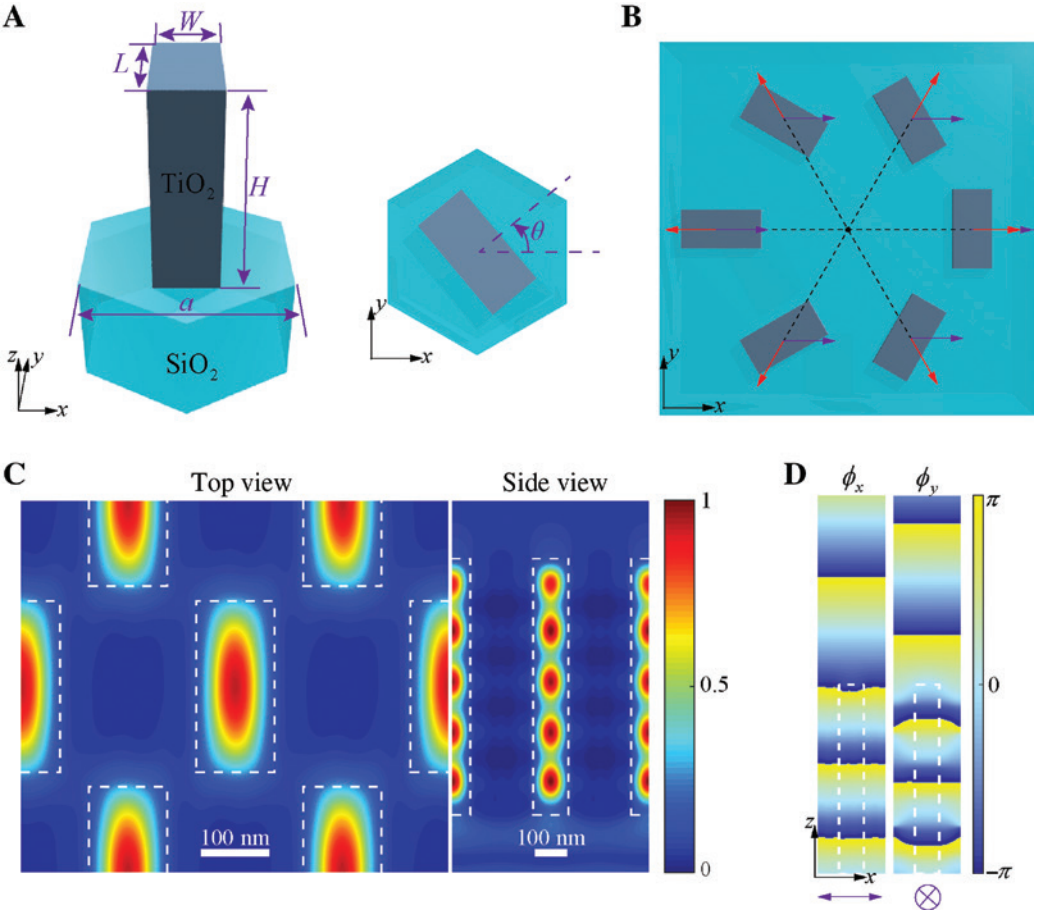

Figure 2: Illustration of the rectangle titanium dioxide nanopost as a half-wave plate with independent response.
(A) Three-dimensional view and top view of the rectangle nanopost. The titanium dioxide nanopost is located on the silicon substrate and arranged in a hexagonal lattice, determined by the lattice constant a, length L, width W, height H, and rotation angle θ of nanoposts. (B) Schematic illustration of converting the *x*-polarized beam (blue arrow) into RPB (red arrow) using the periodic nanopost array. (C) Simulated normalized magnetic field intensity of the periodic array with $a=320$ nm, $L=255$ nm, $W=117$ nm, $H=900$ nm and $\theta=0$, when a plane wave with the wavelength of 532 nm is normally incident from the bottom of substrate. The white frame denotes the location of nanopost. (D) Phase delay ϕ_x, ϕ_y for *x*- and *y*-polarized incident light transmitting the nanopost. The π phase difference between the two different light indicates that each nanopost can be approximated as a half-wave plate.

$$J(\theta)=e^{i(\phi_y+\pi)}\begin{bmatrix}\cos 2\theta & \sin 2\theta\\ \sin 2\theta & -\cos 2\theta\end{bmatrix}, \quad (1)$$

where ϕ_y is the phase delay for the *y*-polarized light transmitting a nanopost when θ is equal to 0. For the *x*-polarized beam ($E^{in}=[1\ 0]^T$), the transmitted light through a single nanopost satisfies

$$E^{out}=J(\theta)E^{in}=e^{i(\phi_y+\pi)}\begin{bmatrix}\cos 2\theta\\ \sin 2\theta\end{bmatrix}, \quad (2)$$

From Eq. (2), one can locally change the polarization of incident light and control the phase delay by using a large number of properly arranged nanoposts. But we should note that phase coverage of 2π for ϕ_y is required for arbitrary phase control.

To achieve phase coverage of 2π for ϕ_y as well as high transmission, we sweep the length and width of a nanopost with fixed height ($H=900$ nm), rotation angle ($\theta=0$) and lattice constant ($a=320$ nm). The transmission T_y and phase delay ϕ_y as functions of length and width are shown in Figure 3A and B, respectively. It is noted that high transmission (more than 90%) and full 2π phase coverage for ϕ_y are possible when the length and width are chosen properly. Similar results for T_x and ϕ_x can also be obtained using the same approach. To determine the length and width of nanoposts that are able to achieve phase difference of π between ϕ_x and ϕ_y, phase difference as a function of length and width is plotted in Figure 3C. Eight kinds of nanoposts with different dimensions are selected as basic nanoposts for the metalens design, which are the markers as shown in Figure 3A–C. Using these eight nanoposts, full 2π phase coverage can be achieved with the interval of π/4. As seen from Figure 3D, eight kinds of nanoposts have high transmission (average transmission of 96.1% and 95.9% for T_x and T_y, respectively) and phase difference of ~π.

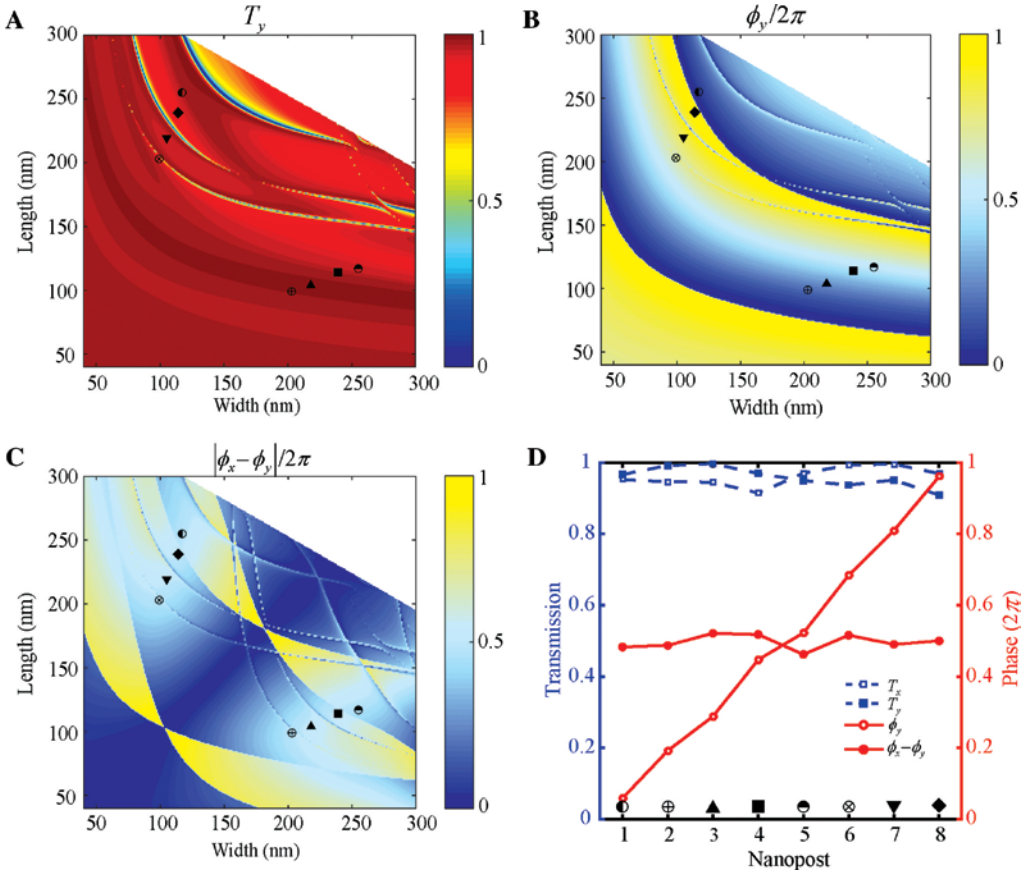

Figure 3: Structural parameters of nanopots for simultaneous control of polarization and phase of the transmitted light. (A,B) Simulated transmission T_y and phase delay ϕ_y as functions of length and width of nanoposts with other fixed parameters, $H=900$ nm, $\theta=0$ and $a=320$ nm. (C) Phase difference between ϕ_x and ϕ_y with variant length and width. (D) The transmission (T_x and T_y), phase delay (ϕ_y) and phase difference ($\phi_x-\phi_y$) of eight selected nanoposts, indicating that all of them have high transmission and phase delay of ~π, and full 2π phase coverage for ϕ_y can be achieved. Blank parts in (A–C) correspond to nanoposts exceeding the boundary of unit cell and are unavailable.

With the selected nanoposts, we are able to achieve polarization and arbitrary phase control by rotating nanoposts and arranging eight kinds of nanoposts in a regular way. To generate RPB using the *x*-polarized light, the rotation angle of the nanoposts can be determined in the way as shown in Figure 2B. Further, the selected nanoposts should be arranged in such a way that the phase profile Φ allows the metalens to focus RPB into a subdiffraction spot.

3 Phase profile design of subdiffraction focusing metalens

In this paper, the phase profile Φ consists of two parts, including the focusing phase profile Φ_{focus} and the filter phase profile Φ_{binary}. Normally, the focusing phase profile is written as

$$\Phi_{focus}(r) = -\frac{2\pi}{\lambda}\left(\sqrt{r^2+f^2}-f\right), \tag{3}$$

where λ = 532 nm is the working wavelength, f = 3.29 μm is the focal length, and $r=\sqrt{x^2+y^2}$ is the radial distance with respect to the center of metalens. On the other hand, the binary phase profile Φ_{binary} is determined by the optimization method. As we know, diffraction theory of bulky lens such as the formulas proposed by Richards et al. [42] has been adopted to optimize the binary phase filter [13–15], but non-negligible deviations would appear when it was used for metalens design. Therefore, in this paper, we develop a metalens diffraction model based on vectorial diffraction theory, which offers a more accurate result for metalenses. The details of metalens diffraction model as well as how to acquire binary phase profile Φ_{binary} based on this model are provided in the following section.

As shown in Figure 4A, RPB with Gaussian intensity distribution is focused by a single-layer metalens. Note

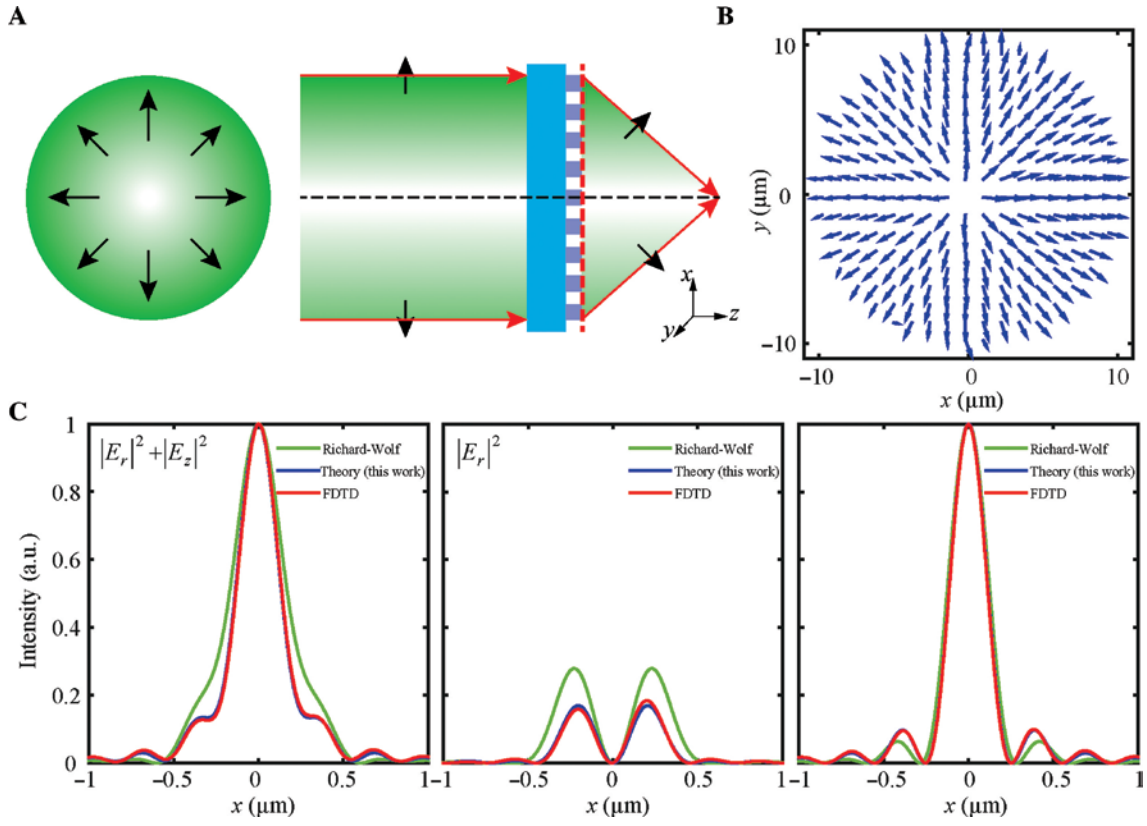

Figure 4: Generation and focusing of radially polarized beam by metalenses.
(A) Schematic illustration of a metalens to focus radially polarized beam with Gaussian intensity distribution. Black and red arrows represent electric field vectors and propagation directions of light, respectively. (B) The polarization profile of radially polarized beam generated by a metalens. (C) Total intensity distribution, radial and longitudinal components of the focal spot are computed by three different methods, Richard-Wolf formulas (green), theoretical model proposed in this paper (blue) and full-wave simulation (red). The intensity is normalized by the maximum of the total intensity distribution.

that RPB can be generated by a metalens composed of nanostructures selected in Figure 3. The generated RPB with high polarization purity (defined as the ratio of electric filed intensity of radial component and total electric field intensity) of 95% is shown in Figure 4B.

In the cylindrical coordinate, the electric field of the incident RPB can be written as

$$\begin{bmatrix} E_{ix}(r,\phi) \\ E_{iy}(r,\phi) \end{bmatrix} = t_i(r)a_i(r)\hat{e}_i, \tag{4}$$

where E_{ix} and E_{iy} are the x and y component of incident RPB, respectively, $t_i(r)=1$ is the phase factor of RPB, $a_i(r)=\exp(-r^2/w^2)$ ($w=30$ μm) is the amplitude distribution and $\hat{e}_i=[\cos\varphi \ \sin\varphi]^T$ denotes the polarization.

When RPB transmits the metalens, the electric field at the plane immediately behind the metalens (red dash line shown in Figure 4A) can be written as

$$\begin{bmatrix} E_{ox}(r,\phi) \\ E_{oy}(r,\phi) \end{bmatrix} = t_o(r)a_o(r)\hat{e}_o, \tag{5}$$

where $t_o(r)=t_i(r)\ \exp[i(\Phi_{\text{focus}}+\Phi_{\text{binary}})]$, We assume that $a_o(r)$ is equal to $a_i(r)$, which is reasonable when the transmission of metalens is close to 1. In addition, $\hat{e}_o$ is equal to $\left[f/\sqrt{r^2+f^2}\cos\varphi, f/\sqrt{r^2+f^2}\sin\varphi\right]^T$ according to Ref. [43].

When the electric field immediately behind the metalens ($z=0$) is known, the electric field distribution at any plane behind the metalens ($z>0$) can be computed by the vectorial angular spectrum [44, 45]. After some derivations, the final theoretical formulas can be written as

$$E_r(r,\varphi,z)=\int_0^\infty A_1(l)\ \exp(i2\pi qz)J_1(2\pi lr)2\pi l dl, \tag{6a}$$

$$E_\varphi(r,\varphi,z)=0, \tag{6b}$$

$$E_z(r,\varphi,z)=i\int_0^\infty \frac{l}{q}A_1(l)\ \exp(i2\pi qz)J_0(2\pi lr)2\pi l dl, \tag{6c}$$

where $A_1(l)=\int_0^\infty t_o(r)a_o(r)\frac{f}{\sqrt{r^2+f^2}}J_1(2\pi lr)2\pi r dr$, l and q represent the frequency component in the radial and longitudinal direction, respectively. $J_0(\cdot)$ and $J_1(\cdot)$ denote zero-order and first-order Bessel function of the first kind, respectively. As seen from Eq. (6), there are only radial and longitudinal components with non-zero intensity. It is also noted that these two components can be rewritten as the first order and zero order Hankel transform, which can be calculated efficiently via fast Hankel transform algorithm [46].

Using this model, the normalized intensity distribution of the focal spot is plotted in Figure 4C. The radial and longitudinal components are also normalized by the maximum of the total intensity distribution, as shown in Figure 4C (the second and third plot). The results from Richard-Wolf formulas and FDTD full-wave simulation are included. By contrast, the theoretical results computed by the proposed model show good agreement with full-wave simulation results, while the results computed by Richard-Wolf formulas deviate from the full-wave simulation results, especially for the radial component (the second plot). These findings indicate that the proposed model is more accurate and suitable for the metalens design compared to Richard-Wolf formulas.

Based on the proposed model, we assume the phase profile Φ_{binary} to be a circularly symmetric and sectionalized function with binary value (0 and π). It can be written as

$$\begin{aligned} &\Phi_{\text{binary}}(r)=0 \text{ or } \pi, \\ &\text{for } r_i<r\le r_{i+1}(0<r_{i+1}=r_i+\Delta_i\le R, \quad i=1,\ 2,\ 3\ \ldots), \end{aligned} \tag{7}$$

where the value of r_i ($i=1,\ 2,\ 3\ \ldots$) is determined by the optimization process. The minimum of Δ_i is set to be 400 nm. R is the radius of the metalens, which is 10 μm in this paper. Binary particle swarm optimization (BPSO) algorithm [47, 48] is adopted to optimize the value of $\Phi_{\text{binary}}(r)$ in each section ($r_i<r<r_{i+1}$). To proceed the optimization efficiency, a two-step optimization process is performed in this paper. To acquire the sharper focal spot in the designated position, the merit function of the first step is defined as

$$\begin{aligned} &\text{Minimize FWHM} \\ &\text{Subject to: } I_{\text{norm}}(z=f)\ge 0.95 \quad \text{for } z_1\le z\le z_2, \end{aligned} \tag{8}$$

where FWHM is the full width at half-maximum of the focal spot. $I_{\text{norm}}(z)$ denotes the normalized intensity along the optical axis for $z_1\le z\le z_2$. The constraint condition $I_{\text{norm}}(z=f)\ge 0.95$ ensures peak intensity is around the focus. The optimized binary phase profile $\Phi_{\text{binary}}^{\text{opt1}}(r)$ in the first step can be considered as the initial value in the second step. The merit function of the second step is defined as

$$\begin{aligned} &\text{Maximize} \quad I(z=f)/I_0(z=f) \\ &\text{Subject to:} \quad I_{\text{norm}}(z=f)\ge 0.95 \quad \text{for } z_1\le z\le z_2, \\ &\qquad\qquad \text{FWHM}\le \text{FWHM}_{\text{obj}} \end{aligned} \tag{9}$$

where $I(z=f)$ and $I_0(z=f)$ represent the intensity at the focus computed by theoretical formulas (Eq. (6)) with and without $\Phi_{\text{binary}}(r)$, respectively. The constraint condition $\text{FWHM}\le\text{FWHM}_{\text{obj}}$ ensures the FWHM of focal spot smaller

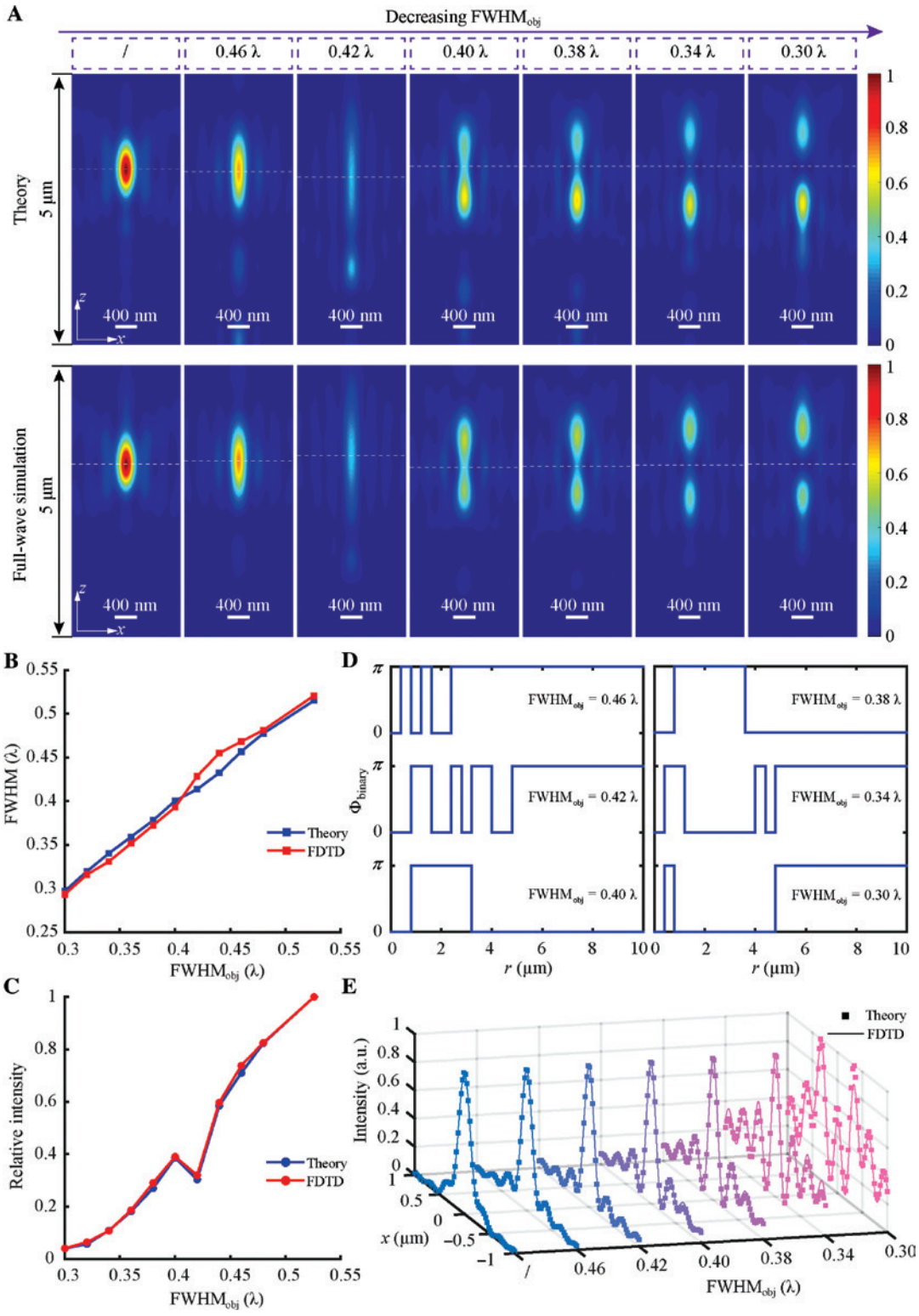

Figure 5: Comparison between theoretical results and simulation results.
(A) Normalized electric field intensity distribution in *x-z* plane calculated by theoretical formulas (top) and full-wave simulation (bottom). The white dashed lines indicate the positions of focuses. The symbol "/" denotes the metalens with the focusing phase but without the optimized binary phase. (B, C) FWHM and relative intensity of the focal spot as functions of FWHM$_{obj}$. (D) Optimized binary phase profiles along radial direction of metalenses at different FWHM$_{obj}$. (E) The *x*-direction cross section (white dashed line in (A)) at different FWHM$_{obj}$.

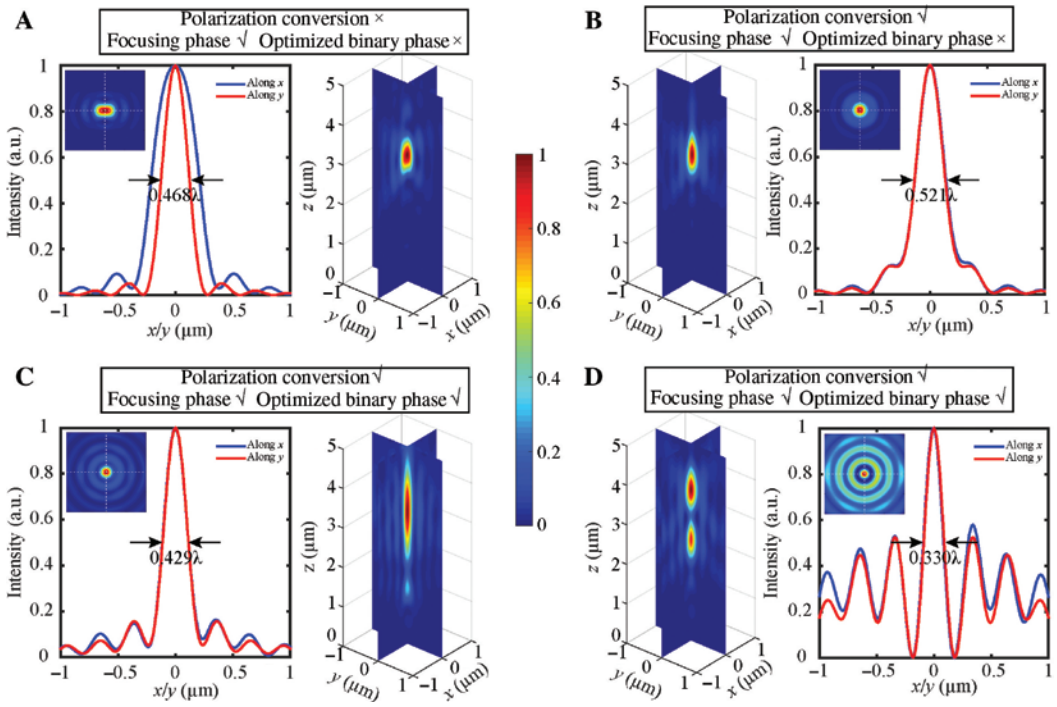

Figure 6: Performance evaluation of the subdiffraction focusing metalens.
Simulated normalized intensity distribution of the focal spot for (A) the metalens without polarization conversion and (B) the metalens without optimization binary phase. Results in (C) and (D) correspond to the metalenses with polarization conversion and optimization binary phase but different preset $FWHM_{obj}$, which are 0.42λ and 0.34λ in (C) and (D), respectively.

than the optimization object $FWHM_{obj}$. After the two-step optimization, we can obtain the final phase profile $\Phi_{binary}(r)$ with different $FWHM_{obj}$.

Using the optimized profiles with a series of decreasing targeted $FWHM_{obj}$, corresponding metalenses are designed. The focal spot for different targeted FWHM is shown in Figure 5A and the corresponding binary phase profiles of these metalenses are shown in Figure 5D. As a comparison, full-wave simulation results are also provided, which shows similar images with theoretical results computed by Eq. (6). It is found that when we decrease the targeted FWHM, the energy in the focal region decreases. When the targeted FWHM is about 0.42λ, we obtain the best focal spot (Figure 5A).

If we continue to decrease the targeted FWHM in the optimization process, the constraint condition cannot be satisfied and when the constraint condition $I_{norm}(z=f) \geq 0.95$ is abandoned, the focal spot splits into two. In these cases, the position of intensity minimum around the designated focal position is defined as the actual focal position. The FWHM and the relative intensity (defined as the ratio of intensity at the focus with optimized binary phase and the intensity at the focus without binary phase) as functions of $FWHM_{obj}$ are plotted in Figure 5B and C. The theoretical results are in good agreement with simulation results. Deviation of FWHM in simulation from that in theory (Figure 5B) is due to boundary shifting of the optimized binary phase caused by discrete sampling of hexagonal unit cells.

As shown in Figure 5B, the FWHM of focal spot can be controlled by changing $FWHM_{obj}$ in the optimization. However, with the decrease of $FWHM_{obj}$, the sidelobes in the focal spot plane increase and even the sidelobes are higher than the main peak for $FWHM_{obj} = 0.30\lambda$, which is reflected in Figure 5E. Such superoscillation phenomenon is consistent with the results illustrated in Refs. [49, 50]. On the other hand, with the decreasing of $FWHM_{obj}$ in Figure 5C, the relative intensity becomes much lower, indicating the low energy in the focal region. Consequently, a compromise between the FWHM and the efficiency should be considered when such metalens is applied in practical applications.

4 Performances of the subdiffraction focusing metalens

To evaluate the performance of subdiffraction focusing metalenses, four kinds of metalenses are compared under

the incidence of *x*-polarized beam, as shown in Figure 6. The first case (Figure 6A) is a metalens with the focusing phase only and a *x*-polarized beam is focused to an elliptic spot with a FWHM 0.468λ in the *y*-direction. This is due to the depolarization effect similar to the phenomenon that happens in high-NA bulky lens [42]. The second case (Figure 6B) is a metalens with polarization conversion and the focusing phase and thus that means a RPB is focused to a circular focal spot with FWHM 0.521λ. The third case is the second case with the extra optimized binary phase profile, which is just the case in the third column of Figure 5A. Compared to the second case, it achieves subdiffraction focusing with FWHM of 0.429λ, as shown in Figures 1B and 6C. The fourth case (Figure 6D) is the superoscillation case in the sixth column of Figure 5A, which has a FWHM 0.33λ with much higher sidelobes. From the above comparison, we conclude that the metalens we design (Figure 6C) can achieve subdiffraction focusing (FWHM = 0.429λ).

Furthermore, the intensity at focus (Eq. (9)) is maximized in the optimization process and a high focusing efficiency value is expected. To characterize the focusing efficiency of the designed metalens, we define the focusing efficiency as the ratio of total electric field intensity in a circular aperture with three times the FWHM of focal spot to the total electric field intensity of incident light, which is commonly used in the metalens design [17, 20]. It is found that the focusing efficiency of the metalens (Figure 6C) is 17.2% compared to 9.5% for superoscillation case in Figure 6D. In addition, they have the close transmission efficiency (defined as the ratio of the power passing through the metalens and the power of incident light), which are 78.1% in Figure 6D and 77.6% in Figure 6C. It should be noted that the focusing efficiency (17.2%) is much higher than the results reported in Refs. [36, 51], leading to a more promising application in superresolution imaging and precision machining.

5 Conclusion

In conclusion, we designed a single-layer metalens to replace bulky optical elements, where the dielectric nanoposts can simultaneously generate RPB and modulate its phase under the incidence of *x*-polarized light. The main contribution of this paper is as follow. First, a theoretical model of planar metalens is developed by virtue of vectorial diffraction theory using RPB. The simulations show that this model provides an efficient way to compute the focusing profile of metalens compared to numerical simulations of solving Maxwell's equation. It also provides an accurate evaluation of metalens focusing profile compared to the diffraction theory associated with bulky lens [37]. Second, a twofold optimization scheme based on the accurate metalens model is presented to optimize the binary phase profile to obtain a subdiffraction spot with high efficiency. Using the optimized binary profile, the designed metalens can achieve subdiffraction focusing (FWHM = 0.429λ) with high transmission efficiency (77.6%) and focusing efficiency (17.2%) when NA = 0.95 and working wavelength is 532 nm. On the other hand, there is a compromise between subdiffraction spot and high focusing efficiency. We may attain the extreme small spot at the expense of low focusing efficiency in the central spot, which corresponds to the superoscillation phenomenon [49].

Compared to traditional bulky optical elements, the subdiffraction focusing metalens we design is miniature and lightweight, which avoids the alignment problem of traditional optical elements. It is expected that this subdiffraction focusing metalens can be integrated in superresolution imaging [7], particle trapping [52], second harmonic generation [53] and Raman spectroscopy [54]. It is possible to further compress the focal spot size by using higher numerical aperture and modulating the amplitude of incident light [14, 15]. What's more, it should be noted that the method used to design the subdiffraction focusing metalens in this paper can also be adopted to design similar metalens at other wavelengths and is able to design a larger metalens to achieve far-field subdiffraction focusing as well.

Acknowledgements: This work was supported by National Natural Science Foundation of China (Grant Nos. 11761161002, 61805288, Funder Id: http://dx.doi.org//10.13039/501100001809), Natural Science Foundation of Guangdong Province (Grant No. 2018B030308005, 2017A030310510, Funder Id: http://dx.doi.org//10.13039/501100003453), and Science and Technology Program of Guangzhou (Grant No. 201804020029, Funder Id: http://dx.doi.org/10.13039/501100004000).

References

[1] Betzig E, Trautman JK, Harris TD, Weiner JS, Kostelak RL. Breaking the diffraction barrier: optical microscopy on a nanometric scale. Science 1991;251:1468–70.
[2] Ito T, Okazaki S. Pushing the limits of lithography. Nature 2000;406:1027–31.
[3] Maragò OM, Jones PH, Gucciardi PG, Volpe G, Ferrari AC. Optical trapping and manipulation of nanostructures. Nat Nanotechnol 2013;8:807–19.

[4] Malinauskas M, Žukauskas A, Hasegawa S, et al. Ultrafast laser processing of materials: from science to industry. Light Sci Appl 2016;5:e16133–46.
[5] Dorn R, Quabis S, Leuchs G. Sharper focus for a radially polarized light beam. Phys Rev Lett 2003;91:233901–4.
[6] Chen R, Agarwal K, Sheppard CJR, Chen X. Imaging using cylindrical vector beams in a high-numerical-aperture microscopy system. Opt Lett 2013;38:3111–4.
[7] Xie X, Chen Y, Yang K, Zhou J. Harnessing the point-spread function for high-resolution far-field optical microscopy. Phys Rev Lett 2014;113:263901–5.
[8] Lerman GM, Levy U. Effect of radial polarization and apodization on spot size under tight focusing conditions. Opt Express 2008;16:4567–81.
[9] Yang L, Xie X, Wang S, Zhou J. Minimized spot of annular radially polarized focusing beam. Opt Lett 2013;38:1331–3.
[10] Kitamura K, Sakai K, Noda S. Sub-wavelength focal spot with long depth of focus generated by radially polarized, narrow-width annular beam. Opt Exp 2010;18:4518–25.
[11] Yew EYS, Sheppard CJR. Tight focusing of radially polarized Gaussian and Bessel-Gauss beams. Opt Lett 2007;32:3417–9.
[12] Lin J, Yin K, Li Y, Tan J. Achievement of longitudinally polarized focusing with long focal depth by amplitude modulation. Opt Lett 2011;36:1185–7.
[13] Wang H, Shi L, Lukyanchuk B, Sheppard C, Chong CT. Creation of a needle of longitudinally polarized light in vacuum using binary optics. Nat Photon 2008;2:501–5.
[14] Guo H, Weng X, Jiang M, et al. Tight focusing of a higher-order radially polarized beam transmitting through multi-zone binary phase pupil filters. Opt Express 2013;21:5363–72.
[15] Nie Z, Shi G, Zhang X, Wang Y, Song Y. Generation of super-resolution longitudinally polarized beam with ultra-long depth of focus using radially polarized hollow Gaussian beam. Opt Commun 2014;331:87–93.
[16] Zha Y, Wei J, Wang H, Gan F. Creation of an ultra-long depth of focus super-resolution longitudinally polarized beam with a ternary optical element. J Opt 2013;15:075703–8.
[17] Arbabi A, Horie Y, Ball AJ, Bagheri M, Faraon A. Subwavelength-thick lenses with high numerical apertures and large efficiency based on high-contrast transmit arrays. Nat Commun 2015;6:7069–74.
[18] Chen WT, Zhu AY, Khorasaninejad M, Shi Z, Sanjeev V, Capasso F. Immersion meta-lenses at visible wavelengths for nanoscale imaging. Nano Lett 2017;17:3188–94.
[19] Fan Z-B, Shao Z-K, Xie M-Y, et al. Silicon nitride metalenses for close-to-one numerical aperture and wide-angle visible imaging. Phys Rev Appl 2018;10:014005–10.
[20] Liang H, Lin Q, Xie X, et al. Ultrahigh numerical aperture metalens at visible wavelengths. Nano Lett 2018;18:4460–6.
[21] Paniagua-Domínguez R, Yu YF, Khaidarov E, et al. A metalens with a near-unity numerical aperture. Nano Lett 2018;18:2124–32.
[22] Khorasaninejad M, Crozier KB. Silicon nanofin grating as a miniature chirality-distinguishing beam-splitter. Nat Commun 2014;5:5386–91.
[23] Lin D, Fan P, Hasman E, Brongersma ML. Dielectric gradient metasurface optical elements. Science 2014;345:298–302.
[24] Zhou Z, Li J, Su R, et al. Efficient silicon metasurfaces for visible light. ACS Photonics 2017;4:544–51.
[25] Balthasar Mueller JP, Rubin NA, Devlin RC, Groever B, Capasso F. Metasurface polarization optics: independent phase control of arbitrary orthogonal states of polarization. Phys Rev Lett 2017;118:113901–5.
[26] Li Z, Kim I, Zhang L, et al. Dielectric meta-holograms enabled with dual magnetic resonances in visible light. ACS Nano 2017;11:9382–9.
[27] Zhao R, Sain B, Wei Q, et al. Multichannel vectorial holographic display and encryption. Light Sci Appl 2018;7:95–103.
[28] Chen WT, Khorasaninejad M, Zhu AY, et al. Generation of wavelength-independent subwavelength Bessel beams using metasurfaces. Light Sci Appl 2017;6:e16259–64.
[29] Yi X, Ling X, Zhang Z, et al. Generation of cylindrical vector vortex beams by two cascaded metasurfaces. Opt Express 2014;22:17207–15.
[30] Arbabi A, Horie Y, Bagheri M, Faraon A. Dielectric metasurfaces for complete control of phase and polarization with subwavelength spatial resolution and high transmission. Nat Nanotechnol 2015;10:937–43.
[31] Chen H, Chen Z, Li Q, Lv H, Yu Q, Yi X. Generation of vector beams based on dielectric metasurfaces. J Mod Opt 2015;62:638–43.
[32] Zhang F, Yu H, Fang J, et al. Efficient generation and tight focusing of radially polarized beam from linearly polarized beam with all-dielectric metasurface. Opt Express 2016;24:6656–64.
[33] Luo J, Zhang Z, Song M, He A, Yu H. Simultaneous generation and focus of radially polarized light with metal-dielectric grating metasurface. Opt Commun 2017;382:421–7.
[34] Zhao R, Huang L, Tang C, et al. Nanoscale polarization manipulation and encryption based on dielectric metasurfaces. Adv Opt Mater 2018;6:1800490–8.
[35] Fan Q, Zhu W, Liang Y, et al. Broadband generation of photonic spin-controlled arbitrary accelerating light beams in the visible. Nano Lett 2019;19:1158–65.
[36] Tang D, Wang C, Zhao Z, et al. Ultrabroadband superoscillatory lens composed by plasmonic metasurfaces for subdiffraction light focusing. Laser Photon Rev 2015;9:713–9.
[37] Zuo R, Liu W, Cheng H, Chen S, Tian J. Breaking the diffraction limit with radially polarized light based on dielectric metalenses. Adv Opt Mater 2018;6:1800795–802.
[38] He Q, Sun S, Xiao S, Zhou L. High-efficiency metasurfaces: principles, realizations, and applications. Adv Opt Mater 2018;6:1800415–37.
[39] Qin F, Ding L, Zhang L, et al. Hybrid bilayer plasmonic metasurface efficiently manipulates visible light. Sci Adv 2016;2:e1501168.
[40] Chen K, Feng Y, Monticone F, et al. A reconfigurable active Huygens' metalens. Adv Mater 2017;29:1606422–9.
[41] Liu V, Fan S. S4: a free electromagnetic solver for layered periodic structures. Comput Phys Commun 2012;183:2233–44.
[42] Richards B, Wolf E, Gabor D. Electromagnetic diffraction in optical systems, II. Structure of the image field in an aplanatic system. Proc R Soc Lond Ser A: Math Phys Sci 1959;253:358–79.
[43] Youngworth KS, Brown TG. Focusing of high numerical aperture cylindrical-vector beams. Opt Express 2000;7:77–87.
[44] Liu P, Lü B. The vectorial angular-spectrum representation and Rayleigh–Sommerfeld diffraction formulae. Opt Laser Technol 2007;39:741–4.
[45] Liu T, Tan J, Liu J, Wang H. Vectorial design of super-oscillatory lens. Opt Express 2013;21:15090–101.

[46] Siegman AE. Quasi fast Hankel transform. Opt Lett 1977;1:13–5.
[47] Kennedy J, Eberhart RC. A discrete binary version of the particle swarm algorithm. In: 1997 IEEE International Conference on Systems, Man, and Cybernetics. Comput Cyber Sim, 12–15 October 1997, vol. 5, pp. 4104–8.
[48] Mojtaba Ahmadieh K, Mohammad T, Mahdi Aliyari S. A novel binary particle swarm optimization. In: 2007 Mediterranean Conference on Control & Automation, 27–29 June 2007, pp. 1–6.
[49] Huang K, Ye H, Teng J, Yeo SP, Luk'yanchuk B, Qiu C-W. Optimization-free superoscillatory lens using phase and amplitude masks. Laser Photon Rev 2014;8:152–7.
[50] Qin F, Huang K, Wu J, Teng J, Qiu C-W, Hong M. A supercritical lens optical label-free microscopy: sub-diffraction resolution and ultra-long working distance. Adv Mater 2017;29:1602721–6.
[51] Kotlyar VV, Nalimov AG, Stafeev SS, et al. Thin high numerical aperture metalens. Opt Express 2017;25:8158–67.
[52] Zhan Q. Trapping metallic Rayleigh particles with radial polarization. Opt Express 2004;12:3377–82.
[53] Biss DP, Brown TG. Polarization-vortex-driven second-harmonic generation. Opt Lett 2003;28:923–5.
[54] Gong L, Lin J, Hao C, et al. Supercritical focusing coherent anti-Stokes Raman scattering microscopy for high-resolution vibrational imaging. Opt Lett 2018;43:5615–8.